

## ORIGINAL ARTICLE

# Homozygous Loss of Autism-Risk Gene CNTNAP2 Results in Reduced Local and Long-Range Prefrontal Functional Connectivity

Adam Liska<sup>1,2</sup>, Alice Bertero<sup>1,3</sup>, Ryszard Gomolka<sup>1</sup>, Mara Sabbioni<sup>4</sup>, Alberto Galbusera<sup>1</sup>, Noemi Barsotti<sup>3</sup>, Stefano Panzeri<sup>5</sup>, Maria Luisa Scattoni<sup>4</sup>, Massimo Pasqualetti<sup>1,3</sup> and Alessandro Gozzi<sup>1</sup>

<sup>1</sup>Functional Neuroimaging Laboratory, Center for Neuroscience and Cognitive Systems @ UniTn, Istituto Italiano di Tecnologia, Rovereto 38068, Italy, <sup>2</sup>CIMeC, Center for Mind/Brain Sciences, University of Trento, Rovereto 38068, Italy, <sup>3</sup>Department of Biology, Unit of Cell and Developmental Biology, University of Pisa, Pisa 56127, Italy, <sup>4</sup>Department of Cell Biology and Neurosciences, Istituto Superiore di Sanità, Neurotoxicology and Neuroendocrinology Section, Rome 00161, Italy and <sup>5</sup>Neural Computation Laboratory, Center for Neuroscience and Cognitive Systems @ UniTn, Istituto Italiano di Tecnologia, Rovereto 38068, Italy

Address correspondence to Alessandro Gozzi, Functional Neuroimaging Laboratory, Center for Neuroscience and Cognitive Systems @ UniTn, Istituto Italiano di Tecnologia, 38068 Rovereto, Italy. Email: alessandro.gozzi@iit.it

## Abstract

Functional connectivity aberrancies, as measured with resting-state functional magnetic resonance imaging (rsfMRI), have been consistently observed in the brain of autism spectrum disorders (ASD) patients. However, the genetic and neurobiological underpinnings of these findings remain unclear. Homozygous mutations in *contactin associated protein-like 2* (CNTNAP2), a neurexin-related cell-adhesion protein, are strongly linked to autism and epilepsy. Here we used rsfMRI to show that homozygous mice lacking *Cntnap2* exhibit reduced long-range and local functional connectivity in prefrontal and midline brain “connectivity hubs.” Long-range rsfMRI connectivity impairments affected heteromodal cortical regions and were prominent between fronto-posterior components of the mouse default-mode network, an effect that was associated with reduced social investigation, a core “autism trait” in mice. Notably, viral tracing revealed reduced frequency of prefrontal-projecting neural clusters in the cingulate cortex of *Cntnap2*<sup>-/-</sup> mutants, suggesting a possible contribution of defective mesoscale axonal wiring to the observed functional impairments. Macroscale cortico-cortical white-matter organization appeared to be otherwise preserved in these animals. These findings reveal a key contribution of ASD-associated gene CNTNAP2 in modulating macroscale functional connectivity, and suggest that homozygous loss-of-function mutations in this gene may predispose to neurodevelopmental disorders and autism through a selective dysregulation of connectivity in integrative prefrontal areas.

**Key words:** autism, CASPR2, DMN, fMRI, mouse

## Introduction

Neuroimaging and postmortem studies have consistently revealed impaired or atypical connectivity across brain regions of autistic spectrum disorders (ASD) patients (Anagnostou and Taylor 2011). These findings have led to the hypothesis that aberrant connectivity patterns might represent a common final pathway or neurobiological pathogenetic correlate of the autistic phenotype to which different ASD etiologies may converge (Just et al. 2012). Although great heterogeneity exists in the sign and distribution of abnormal connectivity across studies and imaging modalities, consistent features indeed appear to emerge, including reduced functional coherence of long-range intrahemispheric cortico-cortical default-mode circuitry, impaired interhemispheric regulation, and possible increase in local and short-range cortico-subcortical coherence (Rane et al. 2015). However, the neurophysiological underpinnings of these connective derangements are largely unknown, and a causal etiopathological contribution of specific genetic variants to impaired connectivity in ASD remains to be firmly established.

Mouse lines recapitulating high-confidence ASD mutations (Sanders et al. 2015) have been employed to understand how specific genetic alterations translate into relevant changes in cells and circuits (Auerbach et al. 2011). The recent optimization of neuroimaging readouts of functional connectivity such as resting-state functional magnetic resonance imaging (rsfMRI) in the mouse (Sforazzini et al. 2014) permits to extend this paradigm to the investigation of the elusive genetic and neurobiological foundations of aberrant connectivity observed in ASD (Liska and Gozzi 2016). The approach leverages on the identification of robust homotopic and distributed rsfMRI connectivity networks in the mouse, including possible homologs of distributed human rsfMRI systems like the salience and default-mode networks (DMN) (Gozzi and Schwarz 2015), and the observation that cyto-architecturally conserved heteromodal cortices in cingulate and retrosplenial regions exhibit similar “hub-like” topological properties in both species (Cole et al. 2010; Liska et al. 2015). Importantly, as mouse rsfMRI measurements rest on the same biophysical principles as corresponding human neuroimaging readouts, this approach has the merit of providing a direct translational bridge across species.

Homozygous loss-of-function mutations in the *contactin associated protein-like 2* gene (*CNTNAP2*) encoding CASPR2, a neuroligin-related cell-adhesion molecule, are strongly linked to autism and epilepsy in consanguineous families (Strauss et al. 2006; Alarcin et al. 2008; Rodenas-Cuadrado et al. 2014). Loss of *Cntnap2* in mice leads to abnormal neuronal migration, reduced GABAergic neurons, spontaneous seizures, and behavioral traits consistent with ASD symptoms in humans (Peñagarikano et al. 2011), an ensemble of traits that phenocopy major neuropathological features observed in cortical dysplasia-focal epilepsy (CDFE) syndrome, a rare neuronal migration disorder associated with a recessive mutation in *CNTNAP2* (Strauss et al. 2006). Interestingly, common genetic variants in *CNTNAP2* were recently described to be associated with impaired frontal lobe connectivity in humans (Scott-Van Zeeland et al. 2010). However, a causal relationship between ASD-related loss-of-function mutations in *CNTNAP2* and functional connectivity remains to be firmly established. Moreover, the role of *CNTNAP2* in shaping macroscale circuit assembly, and the specific substrates affected, remain largely unknown.

To address these questions, we used blood oxygen level-dependent (BOLD) rsfMRI, diffusion-weighted (DW) MRI, and retrograde viral tracing to map large-scale functional connectivity

and white-matter topology in homozygous *Cntnap2*-null mice (*Cntnap2*<sup>-/-</sup>). We document that loss of *Cntnap2* results in local and long-range connectivity reductions affecting prefrontal regions that act as functional connectivity hubs in the mouse brain (Liska et al. 2015), and that fronto-posterior hypoconnectivity is associated with impaired social behavior. The presence of reduced prefrontal-projecting neuronal frequency in the cingulate cortex of *Cntnap2*<sup>-/-</sup> mutants suggest a possible contribution of defective mesoscale axonal wiring to the observed functional connectivity impairments. Collectively, these results reveal a role of autism-risk gene *CNTNAP2* in modulating functional network assembly between key integrative connectivity hubs of the mammalian brain. The observed long-range prefrontal hypoconnectivity in *Cntnap2*<sup>-/-</sup> mice recapitulates imaging findings in autism and adds to the construct validity of this mouse line to model ASD-related phenotypes.

## Materials and Methods

### Ethical Statement

All in vivo studies were conducted in accordance with the Italian law (DL 116, 1992 Ministero della Sanità, Roma) and the recommendations in the Guide for the Care and Use of Laboratory Animals of the National Institutes of Health. Animal research protocols were also reviewed and consented to by the animal care committee of the Istituto Italiano di Tecnologia. The Italian Ministry of Health specifically approved the protocol of this study, authorization no. 07753 to A.G. All surgical procedures were performed under anesthesia.

### Animals

*Cntnap2*-null (*Cntnap2*<sup>-/-</sup>) and control “wild-type” (*Cntnap2*<sup>+/+</sup>) breeding pairs were obtained from Jackson Laboratories and bred locally. Mice were housed by sex in mixed genotype groups, with temperature maintained at 21 ± 1 °C and humidity at 60 ± 10%. All experiments were performed on adult male mice between 12 and 16 weeks of age, corresponding to young maturity. The specific age-range for each experimental activity is reported below. No onset of spontaneous seizures was observed in any of the *Cntnap2* mutants or control mice tested in behavioral, imaging, or tracing studies. This is consistent with previous reports showing propensity for spontaneous epileptic episodes in *Cntnap2*<sup>-/-</sup> to occur only after 6 months of age (Peñagarikano et al. 2011).

### Social Interaction

For behavioral testing, 12-week-old *Cntnap2*<sup>-/-</sup> and control *Cntnap2*<sup>+/+</sup> mice ( $n = 13$  each group) were evaluated in the male-female social interaction test during the light phase, as previously described (Scattoni et al. 2011, 2013). An unfamiliar stimulus control female mouse in estrous was placed into the home-cage of an isolated test male mouse, and social behavior was recorded during a 3-min test session. Scoring of social investigation parameters was conducted using Noldus Observer 10XT software (Noldus Information Technology). Social interactions were defined as number of events (frequency) and duration of the following behavioral responses performed by the test mouse: anogenital sniffing (direct contact with the anogenital area), body sniffing (sniffing or snout contact with the flank area), head sniffing (sniffing or snout contact with the head/neck/mouth area), locomotor activity, rearing up against the wall of the home-cage, digging in the bedding, and grooming

(self-cleaning, licking any part of its own body). Social investigation is defined as the sum of sniffing and following behaviors (Scattoni et al. 2008). No observations of mounting, fighting, tail rattling, and wrestling behaviors were recorded. Scoring was rated by 2 investigators blind to genotype. Interrater reliability was 98%. To measure ultrasound vocalization (USV) recordings, an ultrasonic microphone (Avisoft UltraSoundGate condenser microphone capsule CM16, Avisoft Bioacoustics) was mounted 20 cm above the cage and the USVs were recorded using Avisoft RECORDER software version 3.2. Settings included sampling rate at 250 kHz; format 16 bit. The ultrasonic microphone was sensitive to frequencies between 10 and 180 kHz. For acoustical analysis, recordings were transferred to Avisoft SASLabPro (version 4.40) and a fast Fourier transformation was conducted as previously described (Scattoni et al. 2008). Start times for the video and audio files were synchronized.

### Resting-State fMRI

rsfMRI experiments were performed on the same experimental cohorts employed in the behavioral tests ( $n = 13$  Cntnap2<sup>+/+</sup>;  $n = 13$  Cntnap2<sup>-/-</sup>). At the time of imaging, mice were 13–14 weeks old. The animal preparation protocol was recently described in great detail (Ferrari et al. 2012; Sforazzini et al. 2016). Briefly, mice were anaesthetized with isoflurane (5% induction), intubated, and artificially ventilated (2% maintenance). The left femoral artery was cannulated for continuous blood pressure monitoring and terminal arterial blood sampling. At the end of surgery, isoflurane was discontinued and substituted with halothane (0.75%). Functional data acquisition commenced 45 min after isoflurane cessation. Mean arterial blood pressure was recorded throughout imaging sessions. Arterial blood gases ( $p_a\text{CO}_2$  and  $p_a\text{O}_2$ ) were measured at the end of the functional time series to exclude nonphysiological conditions. Mean  $p_a\text{CO}_2$  and  $p_a\text{O}_2$  levels recorded were  $17 \pm 3$  and  $250 \pm 29$  mmHg in Cntnap2<sup>+/+</sup> and  $15 \pm 3$  and  $231 \pm 38$  mmHg in Cntnap2<sup>-/-</sup>. Possible genotype-dependent differences in anesthesia sensitivity were evaluated using Student's 2-sample t-test applied to 2 independent readouts previously shown to be linearly correlated with anesthesia depth: mean arterial blood pressure and amplitude of cortical BOLD signal fluctuations (Steffey et al. 2003; Liu et al. 2011; Zhan et al. 2014).

rsfMRI images were acquired with a 7.0-T MRI scanner (Bruker Biospin, Milan) as previously described (Liska et al. 2015), using a 72-mm birdcage transmit coil and a 4-channel solenoid coil for signal reception. For each session, high-resolution anatomical images were acquired with a fast spin echo sequence (repetition time (TR)/echo time (TE) 5500/60 ms, matrix  $192 \times 192$ , field of view  $2 \times 2$  cm<sup>2</sup>, 24 coronal slices, slice thickness 0.50 mm). Cocentered single-shot BOLD rsfMRI time series were acquired using an echo planar imaging (EPI) sequence with the following parameters: TR/TE 1200/15 ms, flip angle 30°, matrix  $100 \times 100$ , field of view  $2 \times 2$  cm<sup>2</sup>, 24 coronal slices, slice thickness 0.50 mm, 500 volumes, and a total rsfMRI acquisition time of 10 min. Readers can contact the corresponding author for access to the MRI raw data, templates, and code employed to generate the functional maps.

### Functional Connectivity Analyses

The first 20 volumes of the rsfMRI data were removed to allow for  $T_1$  equilibration effects. The time series were then despiked, corrected for motion, and spatially normalized to an in-house mouse brain template (Sforazzini et al. 2014). The normalized

data had a spatial resolution of  $0.1042 \times 0.1042 \times 0.5$  mm<sup>3</sup> ( $192 \times 192 \times 24$  matrix). Head motion traces and mean ventricular signal (averaged rsfMRI time course within a reference ventricular mask) were regressed out of each of the time series. No intergroup differences in ventricular volume was observed as measured by the dimension of individual ventricular masks (t-test,  $P = 0.31$ ). All rsfMRI time series were spatially smoothed (full width at half maximum of 0.6 mm) and band-pass filtered to a frequency window of 0.01–0.1 Hz.

To obtain an unbiased identification of the brain regions exhibiting genotype-dependent differences in functional connectivity, we implemented recently developed aggregative metrics for these parameters (Cole et al. 2010; Maximo et al. 2013; Liska et al. 2015) and calculated local and global connectivity maps for all subjects. This metric considers connectivity of a given voxel to a subset of all other voxels within the brain mask by computing average connectivity strength. Specifically, we employed the weighted connectivity method, in which individual  $r$ -scores are first transformed to  $z$ -scores using Fisher's  $r$ -to- $z$  transform and then averaged to yield the final connectivity score. Local connectivity strength was mapped by limiting this measurement to connections within a 6-voxel radius sphere (0.6252 mm in plane), while long-range connectivity was computed by considering only connections to voxels outside this sphere. The radius employed represents approximately half the thickness of mouse anterior cortex (Dodero et al. 2013) and is a good approximation of the overall average cortical thickness (Braitenberg and Schüz 1998; Sun and Hevner, 2014). The use of this value ensures that the employed local connectivity metric reflects purely intracortical effects at least in outmost cortical voxels and in thicker fronto-cortical regions. This value is proportionally much lower than what is commonly employed in human local connectivity mappings, where values as large as 14 mm (i.e. 4/5-fold mean human cortical thickness) have been employed (reviewed by Maximo et al. 2013).

Voxelwise intergroup differences in each of these parameters were mapped using a 2-tailed Student's  $t$ -test ( $P < 0.05$  family-wise error [FWE] cluster-corrected, with cluster-defining threshold of  $t_{24} > 2.06$ ,  $P < 0.05$ , as implemented in Jenkinson et al. 2012). The effect was also quantified in volumes of interest (VOIs). The anatomical location of the examined VOIs is reported in Supplementary Figure 1. Region identification and naming follow classic neuroanatomical labeling as described in Paxinos and Franklin (2011). Many of these regions have recently been reclassified according to their cytoarchitectural properties such to match analogous regions in human and primates (Vogt and Paxinos 2014). According to this scheme, the mouse prelimbic cortex corresponds to Brodmann area 32 (A32), cingulate cortex area 1 (anterior cingulate cortex) to Brodmann area A24b, infralimbic cortex to A24a, retrosplenial cortex to areas A30 and A29. In keeping with this and the comparative work of other authors (Öngür and Price 2000), in this paper, we define the mouse prefrontal cortex (PFC) as an anatomical ensemble of regions including prelimbic, infralimbic, and anterior cingulate cortex, corresponding to Brodmann areas A24a/b, A32, and A10.

Intergroup differences in the extension and intensity of long-range rsfMRI correlation networks were mapped using seed-based approach as previously described (Sforazzini et al. 2016). Small a priori seed regions of  $3 \times 3 \times 1$  voxels were chosen to cover anteroposterior cortical networks and representative heteromodal cortical structures (Supplementary Fig. 2). The mean time courses from the unilateral (medial, Rs, and PrL) and bilateral seeds (TeA, Pt, and vHC) were used as regressors

for each voxel. Group-level differences in connectivity distributions were mapped using 2-tailed Student's *t*-tests ( $P < 0.05$  FWE cluster-corrected, with cluster-defining threshold of  $t_{24} > 2.06$ ,  $P < 0.05$ , as implemented in FSL).

Alterations in interhemispheric functional connectivity were assessed by computing correlation coefficients of interhemispheric VOI pairs depicted in Supplementary Figure 1. The statistical significance of intergroup correlation strength in each VOI was assessed with a 2-tailed Student's *t*-test ( $t_{24} > 2.06$ ,  $P < 0.05$ ) and corrected for multiple comparisons using a false discovery rate (FDR)  $q = 0.05$  according to the Benjamini-Hochberg procedure.

Anteroposterior DMN connectivity was mapped by computing seed-to-VOI correlations. Prelimbic and cingulate cortex were employed as prefrontal VOIs. The location of seeds employed for mapping is indicated in Supplementary Figure 2. The statistical significance of intergroup effects was quantified using 2-way repeated-measures ANOVA, where seed location and genotype were used as variables.

### Diffusion MRI

Ex vivo DW MRI was carried out on paraformaldehyde (PFA) fixed specimens as previously described (Doderer et al. 2013). At the end of the rsfMRI experiments, mice were transcardially perfused with 4% PFA under deep isoflurane anesthesia. Brains were imaged inside intact skulls to avoid postextraction deformations. Each DW data set was composed of 8 non-DW images and 81 different diffusion gradient-encoding directions with  $b = 3000 \text{ s/mm}^2$  ( $\delta = 6 \text{ ms}$ ,  $\Delta = 13 \text{ ms}$ ) acquired using an EPI sequence with the following parameters: TR/TE = 13500/27.6 ms, field of view  $1.68 \times 1.54 \text{ cm}^2$ , matrix  $120 \times 110$ , in-plane spatial resolution  $140 \times 140 \mu\text{m}^2$ , 54 coronal slices, slice thickness  $280 \mu\text{m}$ , number of averages 20. Three mice were discarded from the analyses owing to the presence of large susceptibility distortions in the DW images due to the presence of air bubbles following imperfect perfusion procedure. As a result of this, the final number of subjects per group was  $n = 13$  and  $n = 10$ , for *Cntnap2*<sup>+/+</sup> and *Cntnap2*<sup>-/-</sup>, respectively.

### White-Matter Fiber Tractography

The DW data sets were first corrected for eddy current distortions (FSL/eddy\_correct) and skull-stripped (Oguz et al. 2014). The resulting individual brain masks were manually corrected using ITK-SNAP (Yushkevich et al. 2006). Whole brain tractography was performed using MRtrix3 (Tournier et al. 2012) using constrained spherical deconvolution ( $l_{\text{max}} = 8$ , [Tournier et al. 2007]) and probabilistic tracking (iFOD2) with a FOD amplitude cut-off of 0.2. For each data set, the whole brain mask was used as a seed, and a total of 100,000 streamlines were generated.

The corpus callosum and cingulum were selected as tracts of interest, given their major cortico-cortical extension and direct involvement in prefrontal-posterior connectivity (Vogt and Paxinos 2014). The tracts were virtually dissected with waypoint VOIs described in Supplementary Figure 3 using TrackVis (<http://www.trackvis.org/>). Intergroup differences in streamline counts of the tracts were evaluated using a 2-tailed Student's *t*-test ( $t_{21} > 2.08$ ,  $P < 0.05$ ). To provide a visual assessment of fiber distribution across groups, voxelwise parametric fiber density maps were generated using DiPy (Garyfallidis et al. 2014), by determining for each voxel the number of subjects in which at least one streamline of the fiber tract of interest passes through the voxel. For visualization purposes, both the

dissected tracts and group fiber density maps were transformed to the Allen Mouse Common Coordinate Framework, Version 3 (<http://www.brain-map.org/>).

### Rabies Virus Production and Injection

Unpseudotyped recombinant SADΔG-mCherry rabies virus (RV) was produced as described by Osakada and Callaway (2013). Briefly, B7GG packaging cells, which express the rabies envelope G protein, were infected with unpseudotyped SADΔG-mCherry-RV, obtained by courtesy of Prof. Edward Callaway from the Salk Institute. After 5–6 days, the virus was collected, filtrated with  $0.45 \mu\text{m}$  filter, and concentrated by 2 rounds of ultracentrifugation. The titer of the SADΔG-mCherry-RV preparation was established by infecting Hek-293T cells (ATCC cat. no. CRL-11268) with 10-fold serial dilution of viral stock, counting mCherry expressing cells 3 days after infection. The titer was calculated as  $2 \times 10^{11}$  Infective Units (IU)/mL, and the stock was therefore considered suitable for in vivo microinjection. Intracortical RV injections were carried out as previously described (Sforazzini et al. 2016) in adult (12–16-week-old) male *Cntnap2*<sup>-/-</sup> and control *Cntnap2*<sup>+/+</sup> littermates ( $n = 6$ , each group). To this purpose, mice were deeply anesthetized with avertin ( $250 \text{ mg/kg}$ ) and firmly stabilized on a stereotaxic apparatus (Stoelting Inc.). A micro drill (Cellpoint Scientific Inc.) was used to drill holes through the skull. Injections were performed with a Nanofil syringe mounted on an UltraMicroPump UMP3 with a 4-channel Micro4 controller (World Precision Instruments), at a speed of 5 nL/s, followed by a 5–10 min waiting period, to avoid backflow of viral solution and unspecific labeling. One  $\mu\text{L}$  of viral stock solution was injected unilaterally in the left anterior PFC using the following coordinates for injections, expressed in millimeter from bregma: 1.42 from anterior to posterior, 0.3 lateral,  $-1.6$  deep (Paxinos and Franklin 2011).

### Quantification of Retrogradely Labeled Cells

RV-labeled cell quantification and histological analyses were carried out by an operator (A.B.) blind to genotype. After 7 days from viral injection, the animals were transcardially perfused with 4% PFA, brains were dissected, postfixated over night at  $4^\circ\text{C}$ , and vibratome-cut (Leica Microsystems). RV-infected cells were detected by means of immunohistochemistry performed on every other  $100 \mu\text{m}$  thick coronal section, using rabbit antiretroviral fluorescent protein primary antibody (1:500, AbCam), and goat antirabbit HRP secondary antibody (1:500, Jackson ImmunoResearch), followed by 3-3' diaminobenzidine tetrahydrochloride (Sigma Aldrich) staining. Imaging was performed with MacroFluo microscope (Leica). Each picture was then superimposed onto the corresponding Paxinos Atlas Table (Paxinos and Franklin 2011), and cell bodies were plotted according to their anatomical localization. The cells were then assigned to their corresponding brain regions, and final region-based cell population counts were expressed as fraction of the total amount of labeled cells.

### Histological and Immunohistochemical Analysis of White Matter

To histologically assess the presence of microstructural white-matter alterations, we examined immunofluorescence-enhanced coronal brain sections covering anterior callosal regions from adult (12-week-old) male *Cntnap2*<sup>-/-</sup> and control *Cntnap2*<sup>+/+</sup> littermates ( $n = 5$ , each group) after incubation with rat anti-myelin basic protein (MBP) primary antibody (1:1000,

AbCam), followed by donkey antirat 594 secondary antibody (1:500, Thermo Scientific). We also quantified MBP levels as previously described (Mottershead et al. 2003; Richetto et al. 2016). Briefly, 3 representative random images in anterior callosal regions characterized by parallel or transversal fiber extension with respect to the image plane (corpus callosum and forceps minor of the corpus callosum, respectively) were acquired on a Nikon A1 confocal system, equipped with 561 laser diode and appropriate filter for Texas Red fluorophore. Z-stack images (1.5  $\mu\text{m}$  thick) were acquired using an oil-immersion  $\times 60$  plan-apochromat objective at  $1024 \times 1024$  pixel resolution. Callosal image fields were also qualitatively inspected for the presence of intergroup differences in white-matter organization or reduced neuronal packing/density. MBP content was empirically quantified by summing MBP-immunoreactive areas expressed as number of pixels whose values were above the background threshold, calculated as pixel intensity values in areas with no detectable immunostaining, such as cell nuclei or MBP-devoid background.

## Results

### Reduced Local and Long-Range Connectivity in Fronto-Cortical Regions of *Cntnap2*<sup>-/-</sup> Mice

To obtain an unbiased mapping of genotype-dependent differences in functional connectivity, we implemented recently developed aggregative metrics for local and long-range functional connectivity. This analysis revealed foci of significantly reduced

local and long-range connectivity in *Cntnap2*<sup>-/-</sup> mutants with respect to wild-type control subjects (t-test,  $P < 0.05$  FWE cluster-corrected, with cluster-defining threshold of  $t_{24} > 2.06$ ,  $P < 0.05$ ; Fig. 1) encompassing prefrontal (prelimbic and cingulate) and retrosplenial cortices. These same brain regions have been classified both in mice and in humans as “high strength” functional connectivity hubs (Buckner et al. 2009; Cole et al. 2010; Liska et al. 2015), and as such are thought to play a key integrative role in distributed functional networks. Local connectivity reductions appeared to be more widespread than corresponding long-range connectivity deficits (Fig. 1a,c), encompassing involvement of supplementary motor areas surrounding cingulate cortex. The observed local and long-range connectivity reductions were statistically significant also when integrated over a large VOI encompassing the whole cingulate cortex (local connectivity: Cg, t-test,  $t_{24} = 3.11$ ,  $P = 0.005$ , Fig. 1b; long-range connectivity: Cg, t-test,  $t_{24} = 2.26$ ,  $P = 0.03$ , Fig. 1d).

### Long-Range Connectivity Impairments in *Cntnap2*<sup>-/-</sup> Mice Affect Heteromodal Cortical Regions and the DMN

To identify regional targets of the observed long-range connectivity deficits, we probed rsfMRI networks previously shown to involve prefrontal, cingulate, and retrosplenial regions (Sforzini et al. 2014; Gozzi and Schwarz 2015). Seed-based mapping of retrosplenial and anterior cingulate/prelimbic cortex highlighted foci of reciprocal long-range hypoconnectivity along the midline brain axis in *Cntnap2*<sup>-/-</sup> mutants (t-test,  $P < 0.05$  FWE cluster-corrected,

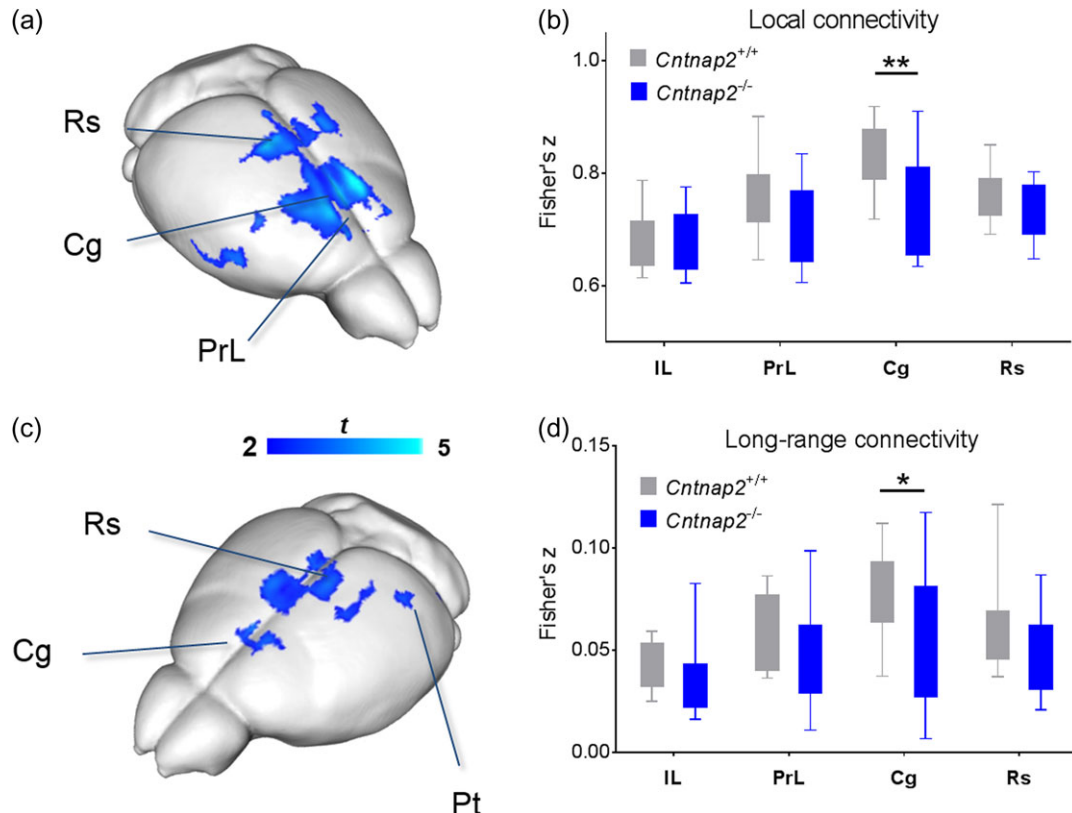


**Figure 1.** Reduced local and long-range connectivity in *Cntnap2*<sup>-/-</sup> mutants. (a) Foci of reduced local connectivity in *Cntnap2*<sup>-/-</sup> versus control *Cntnap2*<sup>+/+</sup> littermates (t-test;  $P < 0.05$  FWE cluster-corrected, with cluster-defining threshold of  $t_{24} > 2.06$ ,  $P < 0.05$ ). (b) Mean local connectivity in regions of interest (t-test; Cg:  $t_{24} = 3.11$ ,  $P = 0.005$ ). (c) Foci of reduced long-range connectivity in *Cntnap2*<sup>-/-</sup> versus control *Cntnap2*<sup>+/+</sup> littermates (t-test;  $P < 0.05$  FWE cluster-corrected, with cluster-defining threshold of  $t_{24} > 2.06$ ,  $P < 0.05$ ). (d) Mean long-range connectivity in regions of interest (t-test; Cg:  $t_{24} = 2.26$ ,  $P = 0.03$ ). IL, infralimbic cortex; PrL, prelimbic cortex; Cg, cingulate cortex; Rs, retrosplenial cortex, \* $P < 0.05$ , \*\* $P < 0.01$ .

with cluster-defining threshold of  $t_{24} > 2.06$ ,  $P < 0.05$ ; Fig. 2a,b). We also probed connectivity of putative lateral components of the rodent DMN such as the posterior parietal and temporal association/auditory cortices, and postero-ventral hippocampus (Gozzi and Schwarz 2015). Parietal cortical mapping revealed foci of reduced local and long-range (middle cingulate) connectivity in *Cntnap2*<sup>-/-</sup> mice (t-test,  $P < 0.05$  FWE cluster-corrected, with cluster-defining threshold of  $t_{24} > 2.06$ ,  $P < 0.05$ ; Fig. 2c). In the same animals, temporal association areas appeared to be widely hypoconnected to retrosplenial, cingulate, and prefrontal regions (t-test,  $P < 0.05$  FWE cluster-corrected, with cluster-defining threshold of  $t_{24} > 2.06$ ,  $P < 0.05$ ; Fig. 2d). We also observed foci of long-range hypoconnectivity between ventral hippocampal and ventral prefrontal (infralimbic) regions (t-test,  $P < 0.05$  FWE cluster-corrected, with cluster-defining threshold of  $t_{24} > 2.06$ ,  $P < 0.05$ ; Fig. 2e). Interhemispheric connectivity in subcortical or motor-sensory

networks appeared to be overall largely preserved. A reduction in interhemispheric connectivity was observed in primary motor areas and visual cortex when quantified in anatomical VOI (Supplementary Fig. 4), although the effect did not survive false discovery rate correction.

Importantly, no genotype-dependent differences in anesthesia sensitivity were detected as seen with mean arterial blood pressure mapping (t-test,  $t_{24} = 0.17$ ,  $P = 0.87$ ; Supplementary Fig. 5a) and amplitude of cortical BOLD signal fluctuations (t-test,  $t_{24} = 0.72$ ,  $P = 0.48$ ; Supplementary Fig. 5b), 2 independent readouts previously shown to be linearly correlated with anesthesia depth (Steffey et al. 2003; Liu et al. 2011). Together with the observation of region-dependent alterations, as opposed to the global reduction described with increased anesthesia dosing (Nasrallah et al. 2014), these findings strongly argue against a confounding contribution of anesthesia to the observed hypoconnectivity.

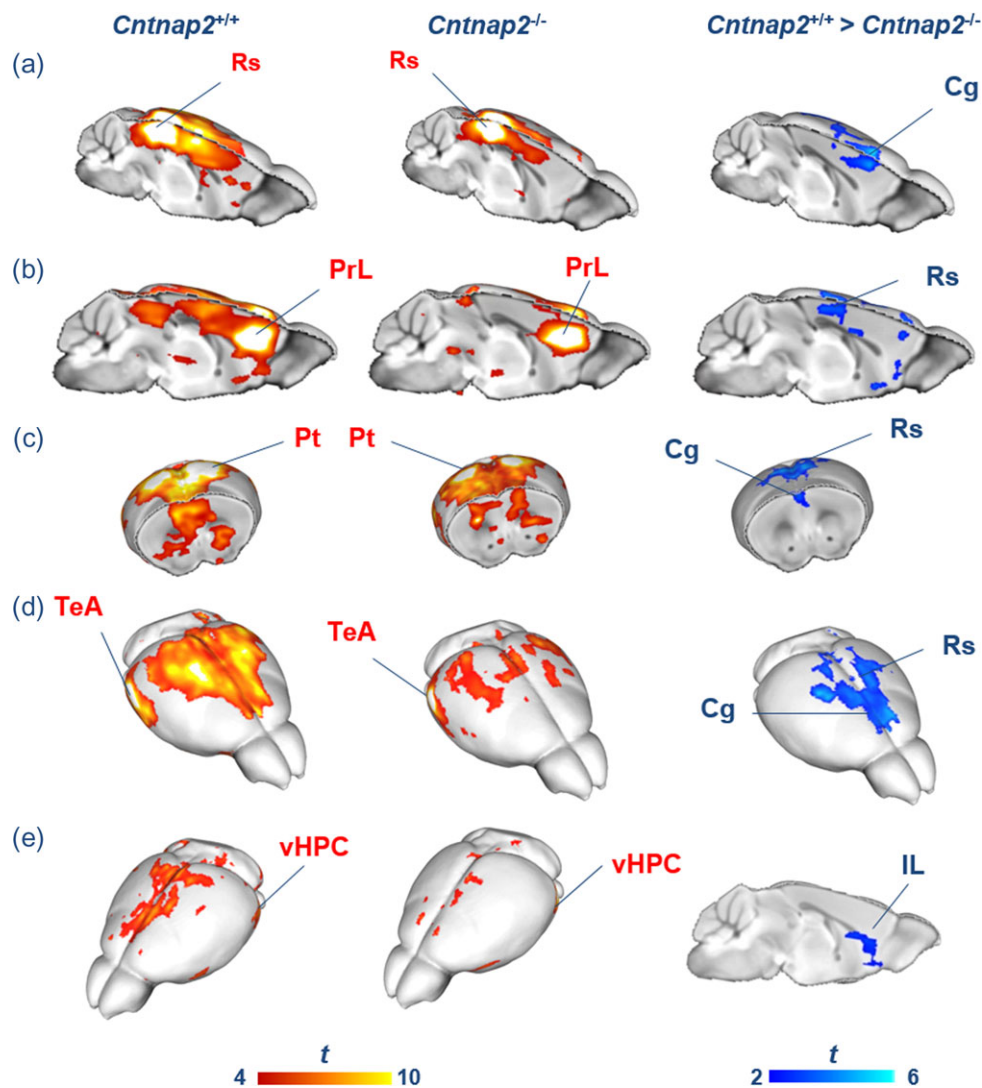


**Figure 2.** Reduced long-range connectivity in *Cntnap2*<sup>-/-</sup> mice. (a–e) Seed-correlation mapping highlighted convergent reduced connectivity between long-range cortical and subcortical regions and cingulate-prefrontal areas. Red/yellow shows areas with significant correlation with seed regions indicated in red (1-sample t-test,  $P < 0.05$  FWE cluster-corrected, with cluster-defining threshold of  $t_{12} > 2.18$ ,  $P < 0.05$ ). Blue indicates foci of reduced connectivity in *Cntnap2*<sup>-/-</sup> mutants with respect to control mice (t-test,  $P < 0.05$  FWE cluster-corrected, with cluster-defining threshold of  $t_{24} > 2.06$ ,  $P < 0.05$ ). Rs, retrosplenial cortex; IL, infralimbic cortex; PrL, prelimbic cortex; Cg, cingulate cortex; Rs, retrosplenial cortex; vHPC, ventral hippocampus; Au/TeA, auditory/temporal association cortices; Pt, parietal cortex.

### Hypoconnectivity in the Mouse DMN is Associated with Impaired Social Behavior

Recent human imaging studies in socially impaired patients have revealed a putative association between long-range DMN hypoconnectivity and social competence (Schreiner et al. 2014). Based on these findings, we hypothesized that reduced long-range DMN connectivity in *Cntnap2*<sup>-/-</sup> mice could be associated with impaired social behavior. To test this hypothesis, we first corroborated DMN hypoconnectivity by quantifying functional connectivity along the dorsal midline axis of this network (anterior/middle cingulate cortex and retrosplenial cortex) using multiple seed-to-VOI measurements (Fig. 3). A clear dysconnection between posterior (retrosplenial) and middle/anterior portions of the DMN (cingulate, prelimbic cortex) was apparent (retrosplenial to cingulate cortex: 2-way repeated-measures ANOVA, genotype effect,  $F_{1,24} = 5.76$ ,  $P = 0.02$ , Fig. 3a; retrosplenial-cingulate to prelimbic: 2-way repeated-measures ANOVA, genotype effect,  $F_{1,24} = 6.82$ ,  $P = 0.02$ , Fig. 3b).

We then measured social behavior in adult *Cntnap2*<sup>-/-</sup> and *Cntnap2*<sup>+/+</sup> control mice in a male-female interaction test, and correlated the measured social scores with DMN hypoconnectivity measures. Consistent with previous reports (Peñagarikano et al. 2011), behavioral testing revealed significantly impaired social interest (total sniffing, duration: t-test,  $t_{24} = 2.29$ ,  $P = 0.03$ , Fig. 4a; social investigation, duration: t-test,  $t_{24} = 2.43$ ,  $P = 0.02$ , Fig. 4c) and increased nonsocial behavior (wall-rearing, frequency: t-test,  $t_{24} = 3.09$ ,  $P = 0.01$ ; Supplementary Fig. 6a) in *Cntnap2*<sup>-/-</sup> mutants compared with *Cntnap2*<sup>+/+</sup> control littermates. Hypoconnectivity in key DMN components (retrosplenial-cingulate cortex) was significantly associated with reduced social behavior (total sniffing, duration:  $r = 0.42$ ,  $P = 0.03$ ,  $n = 26$ ,  $R^2 = 0.17$ , Fig. 4b; social investigation, duration:  $r = 0.40$ ,  $P = 0.04$ ,  $n = 26$ ,  $R^2 = 0.16$ , Fig. 4d) and increased nonsocial behavior (wall-rearing, frequency:  $r = -0.45$ ,  $P = 0.02$ ,  $n = 26$ ,  $R^2 = 0.21$ ;

Supplementary Fig. 6b). These findings highlight a correlation between fronto-posterior connectivity and social behavior, suggesting that impaired functional couplings produced by mutations in *Cntnap2* could reverberate to affect complex behavioral traits such as sociability and social exploration.

### Macroscopic Cortico-Cortical White-Matter Connectivity is Preserved in *Cntnap2*<sup>-/-</sup> Mice

To probe a role of macroscale anatomical connectivity alterations on the observed functional decoupling in *Cntnap2*<sup>-/-</sup>, we performed tractography analysis of the corpus callosum and cingulum, 2 major white-matter tracts characterized by extensive cortico-cortical anteroposterior extension (Fig. 5a). These white-matter tracts appeared to be largely typical in mutant and control mice as seen with group-level fiber density maps (Fig. 5b); in keeping with this, we did not observe statistically significant differences in the number of streamlines between *Cntnap2*<sup>-/-</sup> mutants and controls (cingulum: t-test,  $t_{21} = 1.25$ ,  $P = 0.23$ ; corpus callosum: t-test,  $t_{21} = 1.21$ ,  $P = 0.24$ ; Supplementary Fig. 7). These results argue against a contribution of gross macroscale white-matter alterations to the observed functional connectivity impairments.

### Reduced Prefrontal-Projecting Neuronal Clusters in Cingulate Cortex of *Cntnap2*<sup>-/-</sup> Mice

Although macroscale cortico-cortical connectivity appeared to be normal in *Cntnap2*<sup>-/-</sup> mutants, the possibility exists that finer-scale miswiring, undetectable by tractography, may contribute to the mapped functional connectivity alterations. To probe this hypothesis, we carried out monosynaptic retrograde tracing of the left PFC (prelimbic/anterior cingulate cortex area 1, corresponding to Brodmann area 24Ab, Vogt and Paxinos, 2014)

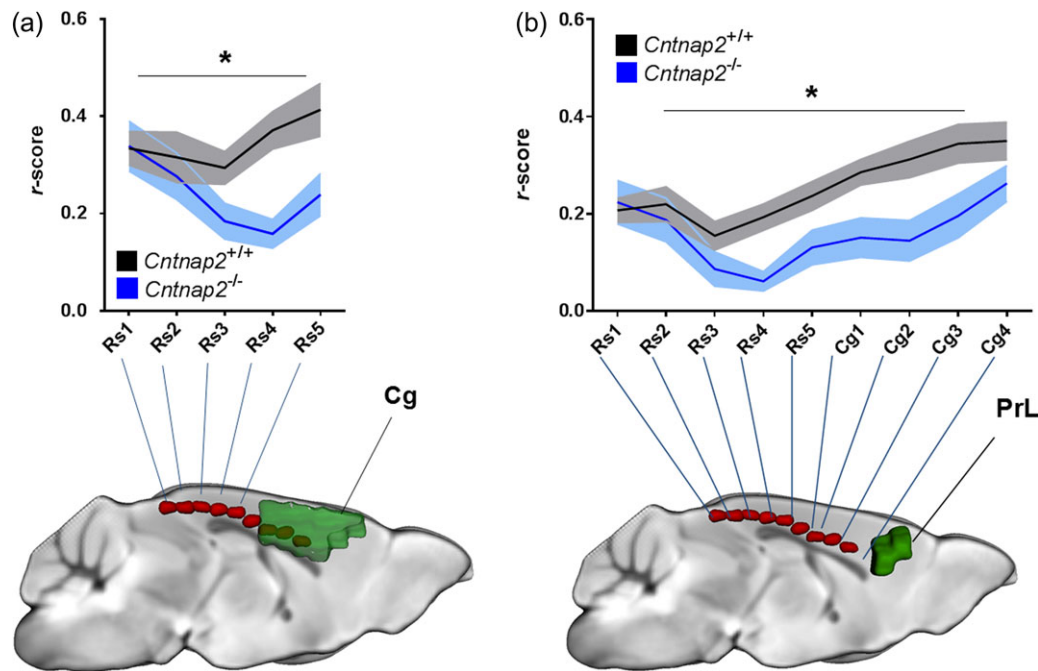


**Figure 3.** Fronto-posterior hypoconnectivity in *Cntnap2*<sup>-/-</sup> mice. (a) Connectivity profile between a series of retrosplenial seeds (Rs, red) and the cingulate cortex (Cg, green) (2-way repeated-measures ANOVA, genotype effect,  $F_{1,24} = 5.76$ ,  $P = 0.02$ ). (b) Connectivity profile between a series of retrosplenial/cingulate seeds (Rs, Cg, red) and the prelimbic cortex (PrL, green) (2-way repeated-measures ANOVA, genotype effect,  $F_{1,24} = 6.82$ ,  $P = 0.02$ ). \* $P < 0.05$ .

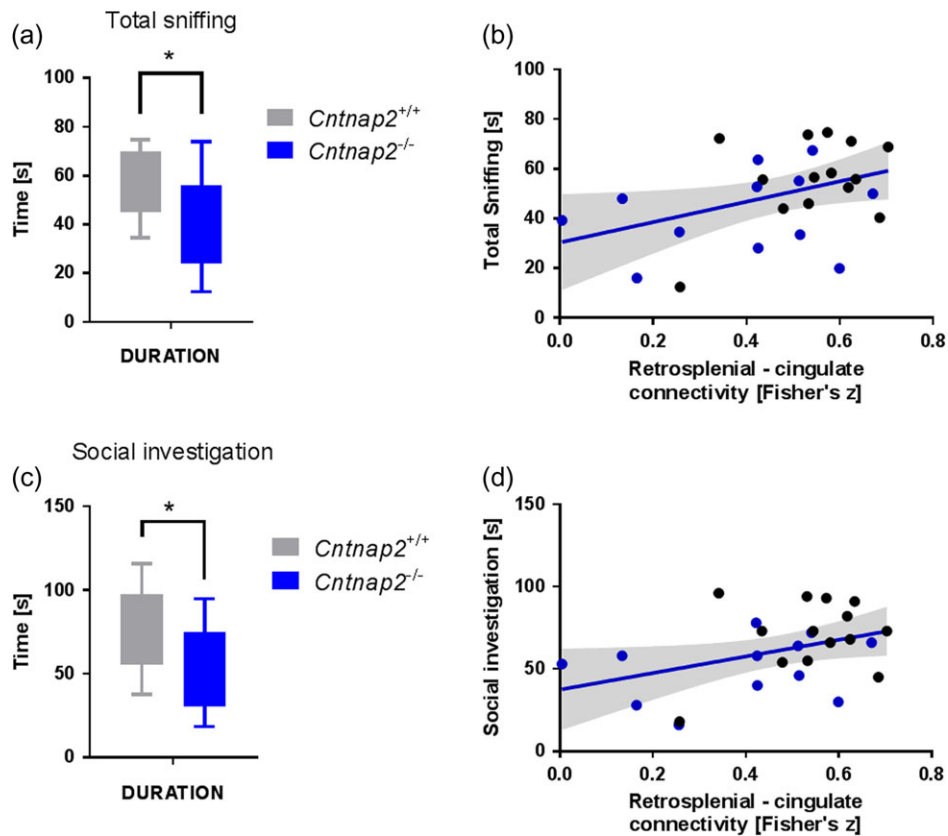


**Figure 4.** Fronto-posterior connectivity is correlated with social behavior. (a) Social behavior as measured by total sniffing duration (t-test,  $t_{24} = 2.29$ ,  $P = 0.03$ ). (b) Association between retrosplenial-cingulate connectivity (VOI-to-VOI) and total sniffing duration ( $r = 0.42$ ,  $P = 0.03$ ,  $n = 26$ ,  $R^2 = 0.17$ ). (c) Social behavior as measured by the duration of social investigation (t-test,  $t_{24} = 2.43$ ,  $P = 0.02$ ). (d) Association between retrosplenial-cingulate connectivity (VOI-to-VOI) and the duration of social investigation ( $r = 0.40$ ,  $P = 0.04$ ,  $n = 26$ ,  $R^2 = 0.16$ ). \* $P < 0.05$ .

and quantified the number of retrogradely labeled cells in representative VOIs in mutant and control littermate mice (Fig. 6a). The anatomical distribution of retrogradely labeled neurons in both genotypes was in keeping with previously published rodent studies (Hoover and Vertes 2007) and encompassed several key anatomical substrates considered to be part of the rodent DMN (Gozzi and Schwarz 2015). Notably, regional quantification of the relative fraction of labeled cells revealed reduced frequency of prefrontal-projecting neurons in the cingulate cortex of *Cntnap2*<sup>-/-</sup> mutants (Cg: t-test,  $t_{10} = 3.90$ ,  $P = 0.003$ , FDR-corrected  $P = 0.04$ ; Fig. 6b,c). Importantly, no genotype-dependent significant difference in the number of prefrontal-projecting neurons was observed in any of the other cortical or subcortical regions examined (Fig. 6b).

#### Preserved Microscale White-Matter Organization in *Cntnap2*<sup>-/-</sup> Mice

We next examined the presence of microscale white-matter structural abnormalities in control and *Cntnap2*<sup>-/-</sup> mutants via histological examinations and MBP quantification. In keeping with previous investigations (Poliak et al. 2003; Peñagarikano et al. 2011), we did not observe gross microscale white-matter disorganization or morphological changes in mice lacking *Cntnap2* with respect to control littermates (Supplementary Fig. 8a). Similarly, MBP quantification in frontal callosal white-matter tracts did not reveal any significant between-group difference (corpus callosum: t-test,  $t_8 = 0.84$ ,  $P = 0.42$ ; forceps

minor of the corpus callosum: t-test,  $t_8 = 1.06$ ,  $P = 0.32$ ; Supplementary Fig. 8b).

#### Discussion

Here we show that homozygous mice lacking *Cntnap2*, a neurixin superfamily member associated with autism, exhibit reduced long-range and local functional connectivity in prefrontal cortical regions and midline functional hubs of the mouse brain, an effect that may involve defective cingulate-prefrontal mesoscale wiring. We also show that reduced fronto-posterior connectivity is associated with impaired social behavior, revealing a possible link between long-range functional connectivity alterations and mouse behavioral traits recapitulating ASD symptoms. Collectively, these findings suggest that loss-of-function mutations in *Cntnap2* may predispose to neurodevelopmental disorders and autism through dysregulation of macroscale functional network couplings.

Our use of an imaging readout widely employed in human connectivity mapping provides us with the opportunity to cross-compare connectivity findings across species. In this respect, the observation of long-range fronto-posterior hypoconnectivity in *Cntnap2*<sup>-/-</sup> mice is especially noteworthy, because it is in excellent agreement with the results of a recent human imaging study where an association between common genetic variants in *CNTNAP2* and similar long-range frontal hypoconnectivity was described (Scott-Van Zeeland et al. 2010). Our results expand these findings, by revealing a causal contribution of *Cntnap2* loss-of-function mutations to long-range

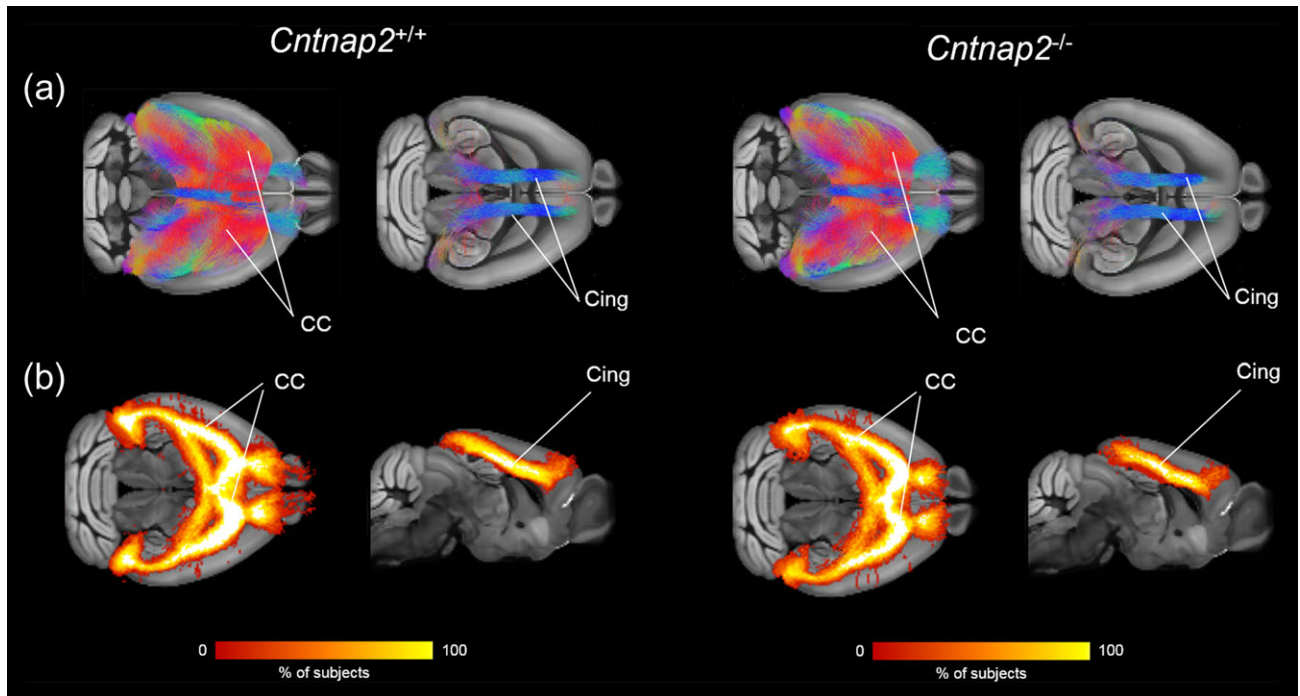


**Figure 5.** Preserved cortico-cortical white-matter organization in *Cntnap2*<sup>-/-</sup> mutants. (a) Corpus callosum and cingulum tracts virtually dissected in 2 representative subjects (*Cntnap2*<sup>+/+</sup> left, *Cntnap2*<sup>-/-</sup> right). (b) Fractional group fiber density maps for corpus callosum and cingulum tracts (*Cntnap2*<sup>+/+</sup> left, *Cntnap2*<sup>-/-</sup>, right).

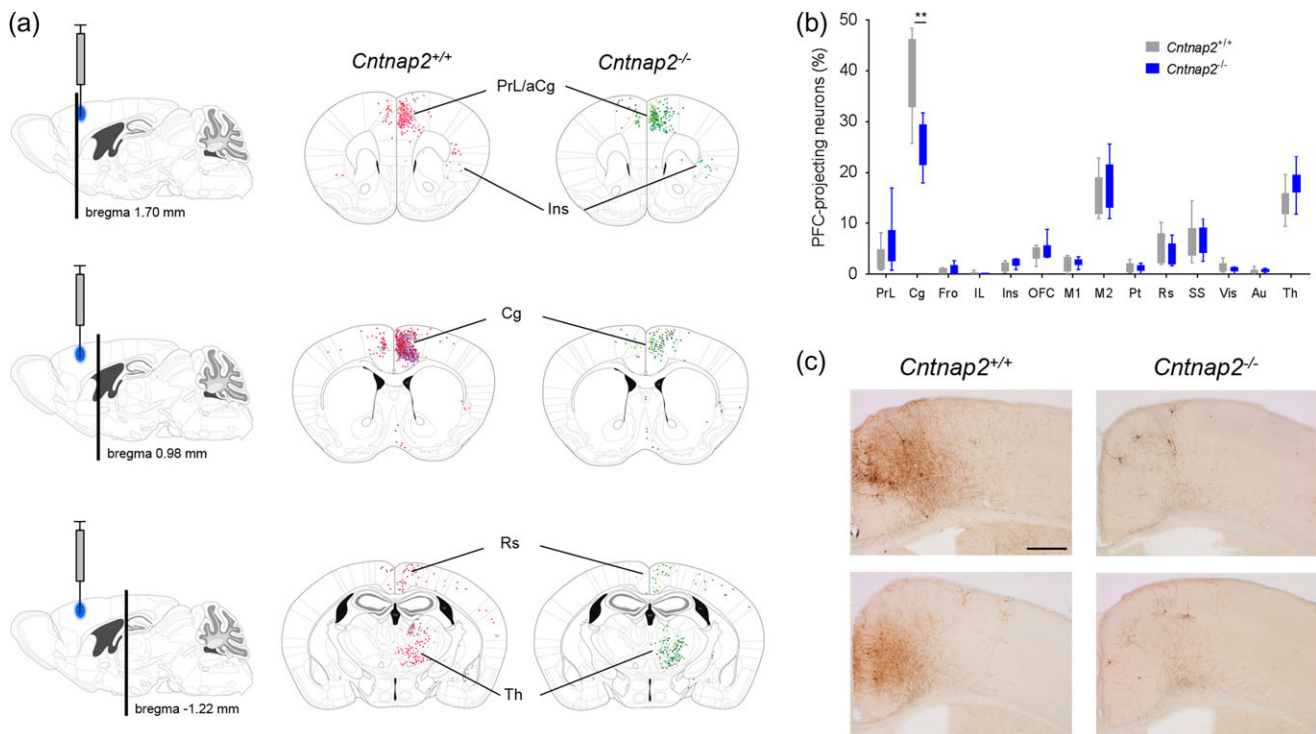


**Figure 6.** Reduced frequency of cingulate-prefrontal-projecting neurons in *Cntnap2*<sup>-/-</sup> mice. (a) Locations of retrogradely labeled cells superimposed on the corresponding Paxinos Atlas coronal tables. Injection location is indicated in blue on the sagittal tables. (b) Regional quantification of the relative regional number (frequency) of retrogradely labeled cells (t-test; Cg:  $t_{10} = 3.90$ ,  $P = 0.003$ , FDR-corrected  $P = 0.04$ ). (c) Enlarged view of the distribution of retrogradely labeled cells in a coronal section of the cingulate region (bregma 0.98 mm) in 2 representative *Cntnap2*<sup>+/+</sup> and 2 *Cntnap2*<sup>-/-</sup> subjects. The scale bar indicates 250  $\mu\text{m}$ . \* $P < 0.05$ , \*\* $P < 0.01$ .

fronto-cortical connectivity impairments. These correspondences also serve as an important proof-of-concept demonstration that ASD-related genetic mutations can lead to

comparable macroscale connectivity deficits in humans and lower mammal species like the laboratory mouse. The presence of long-range hypoconnectivity in *Cntnap2*<sup>-/-</sup> mice also adds to

the remarkable construct and face validity of this mouse model as an experimental tool for mechanistic and therapeutic investigation of syndromic forms of ASD (Peñagarikano et al. 2011). Specifically, *Cntnap2*<sup>-/-</sup> mice closely recapitulate major neuropathological features observed in CDFE syndrome, a rare neuronal migration disorder associated with a recessive (suggesting loss-of-function) mutation in *CNTNAP2*, and, in nearly two-thirds of patients, with autism (Strauss et al. 2006). These include behavioral deficits in the 3 core domains of ASD (reduced vocal communication, repetitive and restricted behaviors, and abnormal social interactions), hyperactivity, and epileptic seizures (both features described in CDFE patients), and reduced GABAergic interneurons, resulting in asynchronous cortical activity as measured with in vivo 2-photon calcium imaging (Peñagarikano et al. 2011).

The observation of defective mesoscale axonal wiring in the cingulate cortex corroborates the presence of selective prefrontal dysregulation in *Cntnap2*<sup>-/-</sup> mutants, and serves as a possible neuroanatomical correlate for some of the prefrontal functional connectivity impairments mapped with rsfMRI. Regional differences in GABAergic interneuron density, and developmental processes related to circuit and network refinements (Zhan et al. 2014; Riccomagno and Kolodkin 2015) are, however, likely to play a role in the observed functional desynchronization as well, given the established contribution of GABAergic oscillatory rhythms in mediating large-scale functional synchrony (Gonzalez-Burgos and Lewis 2008) and the recent evidence of altered spine density and increased spine eliminations in *Cntnap2*<sup>-/-</sup> mice (Gdalyahu et al. 2015). The relative contribution of anatomical versus neurophysiological mechanisms in determining the observed desynchronization remains however undetermined, and interventional studies entailing the regional manipulation of excitatory/inhibitory ratio or inactivation of projection-specific pathways may be required to disambiguate this issue.

Recent human studies described possible microstructural white-matter alterations in carriers of *CNTNAP2* mutations as assessed with water diffusion anisotropy. Specifically, gender-dependent reductions in fractional anisotropy (FA) in the inferior fronto-occipital fasciculus or anterior thalamic radiation have been described by Tan and colleagues (2010). Similarly, Clemm von Hohenberg (2013) described an interaction between a single genotype (rs2710126) and FA, in which homozygotes for the risk allele showed reduced FA values in uncinate fasciculus. These preliminary results suggest the presence of possible white-matter microstructural alterations as a result of *CNTNAP2* gene mutations. However, anisotropic water diffusion reflects multiples biophysical contributions that prevent an unequivocal microstructural interpretation of these findings. For example, reduced FA could be the result of reduced neuronal packing, myelination, axonal diameter, neuronal integrity, and maturation, as well as regional differences in gray matter fraction (Beaulieu, 2014).

To investigate potential microstructural white-matter disruption at a more detailed level than permitted by diffusion MRI, we carried out a histological assessment of white-matter fibers using MBP immunofluorescence. We did not observe any gross white-matter microstructural abnormality in *Cntnap2*<sup>-/-</sup> mutants in terms of fiber orientation, packing, or organization. Moreover, MBP quantification did not reveal any significant genotype-dependent differences. Together with previous electron microscopy investigations, where normal myelin thickness was reported in *Cntnap2*<sup>-/-</sup> mutants (Poliak et al. 2003), these findings argue against the presence of gross microscale white-matter alterations

in these mutants. While this finding appears to be in contrast with human investigations of *CNTNAP2* polymorphisms and suggestive of possible species-specific divergence, additional research is required to more thoroughly investigate the presence of white-matter microstructural aberrancies in *Cntnap2*<sup>-/-</sup> mutants. It should also be noted that *CNTNAP2* polymorphisms studies in humans are typically correlative and involve small patient samples, which make them more prone to confounding factors related to heterogeneity in clinical samples, and individual adaptive differences in microstructural parameters (Scholz et al. 2009).

The observation of hypoconnectivity in prefrontal hub regions of the DMN (Liska et al. 2015) is suggestive of a deficient “maturation” of this functional network (Supekar et al. 2010), and is in keeping with the hypothesis of a key role of this region as a mediator of deficits in global perception and its cognitive representations in ASD patients (Martínez-Sanchis 2014). The notion that “underconnectivity” may preferentially affect complex cognitive and social functions and their higher-order cortical substrates rather than low-level sensory and perceptual tasks has recently found some theoretical support (Kana et al. 2011). Within this framework, heteromodal integrative hubs like the anterior cingulate and PFC, as well as retrosplenial regions would serve as major points of vulnerability for the stability of distributed functional network couplings. rsfMRI mapping in additional mouse lines harboring ASD-related genetic mutations will be instrumental in assessing whether the observed alterations represent a generalizable endophenotype that may converge across mutations and genetic etiologies, or are the specific consequence of *Cntnap2* mutations. It is, however, interesting to note that so far hypoconnectivity appears to be predominant in mouse imaging studies of ASD: reduced connectivity in several brain regions including the PFC and the DMN has been observed in the BTBR model of idiopathic autism (Sforazzini et al. 2016), and in mice characterized by reduced synaptic pruning (Zhan et al. 2014), a pathological trait associated with autism (Tang et al. 2014). Reduced connectivity between motor-sensory regions and a general reduction in primary visual cortex connectivity were also recently described in a mouse model of fragile X syndrome (Haberl et al. 2015). Although preliminary, these initial mouse findings are consistent with and somehow support the “underconnectivity theory” of autism, according to which reduced functional connectivity, at least in the adult brain (Uddin et al. 2013), may emerge as a dominant feature of ASD in the face of heterogeneous etiopathological pathways (Di Martino et al. 2014; Uddin et al. 2013).

In contrast with our imaging results, human rsfMRI mapping in *CNTNAP2* common variant carriers revealed increased, instead of decreased, local connectivity in lateral prefrontal regions (Scott-Van Zeeland et al. 2010). The reason behind this discrepancy is not clear, although several important experimental factors, including methodological, species- and/or age-related differences may contribute to this inconsistency. For example, local connectivity was found to be increased in human lateral prefrontal areas, a region that does not have a clear cytoarchitectural correlate in rodents (Vogt and Paxinos 2014). Moreover, our study was performed in adult male subjects, while human mapping was carried out in prepubertal subjects (mean age 12 years old), a discrepancy that could account for the differences in local connectivity alterations. Indeed, a dramatic reorganization of large-scale functional brain networks occurs during childhood and late adolescence in humans, involving developmental shifts from short-range to long-range connectivity, notably within fronto-insular and cortico-subcortical networks (reviewed by Ernst et al. 2015).

Moreover, an age-related dichotomy has been suggested in ASD-related connectivity aberrancies, with generally reduced intrinsic functional connectivity in adolescents and adults with autism compared with age-matched controls, and increased functional connectivity in younger children with the disorder (Uddin et al. 2013). A similar age-related shift could therefore possibly explain the discrepant direction of local connectivity observed in our study with respect to the finding reported by Scott-Van Zeeland et al. (2010) in human pre-adolescent subjects. Longitudinal investigations of connectivity in rodent genetic models of autism are highly warranted to enable empirical testing of the developmental trajectory of ASD-related connectivity aberrancies across development and network maturation (Liska and Gozzi 2016). Finally, differences in the nature of the investigated mutations should also not be neglected, as the functional consequences of the genetic variants imaged by Scott-Van Zeeland et al. (2010) are unclear, and the possibility that not all the imaged genetic variants are loss-of-function cannot be ruled out.

We also note here that our study specifically addressed male mice only, owing to the greater ASD incidence in this gender (Lai et al. 2015). While this choice has the advantage of reducing within-group variation and subsequent increase in statistical power of our measurements, this should be considered a limitation of our study, as it does not permit to assess whether our findings can be generalized to female carriers of *Cntnap2* loss-of-function mutations.

In conclusion, we document that the absence of *Cntnap2* leads to functional connectivity reductions and defective meso-scale wiring in prefrontal functional hubs of the mouse brain, an effect associated with impaired social behavior. These findings suggest that loss-of-function mutations in *Cntnap2* may predispose to neurodevelopmental disorders and autism through selective dysregulation of connectivity in integrative prefrontal areas, and provide a translational model for investigating connective perturbations in syndromic ASD forms.

## Supplementary Material

Supplementary material can be found at *Cerebral Cortex* online.

## Funding

The study was funded by grants from the Simons Foundation (SFARI 314688 and 400101, A.G.).

## Notes

*Conflict of Interest:* The authors declare that they have no conflict of interest.

## References

- Alarcin M, Abrahams BS, Stone JL, Duvall JA, Perederiy JV, Bomar JM, Sebat J, Wigler M, Martin CL, Ledbetter DH. 2008. Linkage, association, and gene-expression analyses identify CNTNAP2 as an autism-susceptibility gene. *Am J Hum Genet.* 82:150–159.
- Anagnostou E, Taylor M. 2011. Review of neuroimaging in autism spectrum disorders: what have we learned and where we go from here. *Mol Autism.* 2:4.
- Auerbach BD, Osterweil EK, Bear MF. 2011. Mutations causing syndromic autism define an axis of synaptic pathophysiology. *Nature.* 480:63–68.
- Beaulieu C. 2014. The biological basis of diffusion anisotropy. In: Johansen-Berg H, Behren TEJ, editors. *Diffusion MRI: From quantitative measurement to in vivo neuroanatomy.* London, UK; Waltham, MA: Elsevier/Academic Press. p. 155–183.
- Braitenberg V, Schüz A. 1998. *Cortex: statistics and geometry of neuronal connectivity.* Berlin, New York: Springer.
- Buckner RL, Sepulcre J, Talukdar T, Krienen FM, Liu HS, Hedden T, Andrews-Hanna JR, Sperling RA, Johnson KA. 2009. Cortical hubs revealed by intrinsic functional connectivity: mapping, assessment of stability, and relation to Alzheimer's disease. *J Neurosci.* 29:1860–1873.
- Clemm von Hohenberg C, Wigand MC, Kubicki M, Leicht G, Giegling I, Karch S, Hartmann AM, Konte B, Friedl M, Ballinger T, et al. 2013. CNTNAP2 polymorphisms and structural brain connectivity: a diffusion-tensor imaging study. *J Psychiatr Res.* 47:1349–1356.
- Cole MW, Pathak S, Schneider W. 2010. Identifying the brain's most globally connected regions. *NeuroImage.* 49:3132–3148.
- Di Martino A, Yan CG, Li Q, Denio E, Castellanos FX, Alaerts K, Anderson JS, Assaf M, Bookheimer SY, Dapretto M, et al. 2014. The autism brain imaging data exchange: towards a large-scale evaluation of the intrinsic brain architecture in autism. *Mol Psychiatry.* 19:659–667.
- Dodero L, Damiano M, Galbusera A, Bifone A, Tsafaris SA, Scattoni ML, Gozzi A. 2013. Neuroimaging evidence of major morpho-anatomical and functional abnormalities in the BTBR T+TF/J mouse model of autism. *PLoS ONE.* 8:e76655.
- Ernst M, Torrisi S, Balderston N, Grillon C, Hale EA. 2015. fMRI functional connectivity applied to adolescent neurodevelopment. *Annu Rev Clin Psychol.* 11:361–377.
- Ferrari L, Turrini G, Crestan V, Bertani S, Cristofori P, Bifone A, Gozzi A. 2012. A robust experimental protocol for pharmacological fMRI in rats and mice. *J Neurosci Methods.* 204: 9–18.
- Garyfallidis E, Brett M, Amirbekian B, Rokem A, Van Der Walt S, Descoteaux M, Nimmo-Smith I, Dipy Contributors. 2014. Dipy, a library for the analysis of diffusion MRI data. *Front Neuroinform.* 8:8.
- Gdalyahu A, Lazaro M, Penagarikano O, Golshani P, Trachtenberg JT, Geschwind DH. 2015. The autism related protein contactin-associated protein-like 2 (CNTNAP2) stabilizes new spines: an *In Vivo* mouse study. *PLoS ONE.* 10: e0129638.
- Gonzalez-Burgos G, Lewis DA. 2008. GABA neurons and the mechanisms of network oscillations: implications for understanding cortical dysfunction in schizophrenia. *Schizophr Bull.* 34:944–961.
- Gozzi A, Schwarz AJ. 2015. Large-scale functional connectivity networks in the rodent brain. *NeuroImage.* 127:496–509. doi: 10.1016/j.neuroimage.2015.12.017.
- Haberl MG, Zerbi V, Veltien A, Ginger M, Heerschap A, Frick A. 2015. Structural-functional connectivity deficits of neocortical circuits in the *Fmr1*<sup>1G<sup>+</sup>ΔE/y</sup> mouse model of autism. *Sci Adv.* 1:e1500775.
- Hoover W, Vertes R. 2007. Anatomical analysis of afferent projections to the medial prefrontal cortex in the rat. *Brain Struct Funct.* 212:149–179.
- Jenkinson M, Beckmann CF, Behrens TE, Woolrich MW, Smith SM. 2012. FSL. *NeuroImage.* 62:782–790.
- Just MA, Keller TA, Malave VL, Kana RK, Varma S. 2012. Autism as a neural systems disorder: a theory of frontal-posterior underconnectivity. *Neurosci Biobehav Rev.* 36: 1292–1313.

- Kana RK, Libero LE, Moore MS. 2011. Disrupted cortical connectivity theory as an explanatory model for autism spectrum disorders. *Phys Life Rev.* 8:410–437.
- Lai M-C, Lombardo MV, Auyeung B, Chakrabarti B, Baron-Cohen S. 2015. Sex/Gender Differences and Autism: Setting the Scene for Future Research. *J Am Acad Child Adolesc Psychiatry.* 54:11–24.
- Liska A, Gozzi A. 2016. Can mouse imaging studies bring order to autism connectivity chaos? *Front Neurosci.* 10:484.
- Liska A, Galbusera A, Schwarz AJ, Gozzi A. 2015. Functional connectivity hubs of the mouse brain. *Neuroimage.* 115:281–291.
- Liu X, Zhu XH, Zhang Y, Chen W. 2011. Neural origin of spontaneous hemodynamic fluctuations in rats under burst-suppression anesthesia condition. *Cereb Cortex.* 21:374–384.
- Martínez-Sánchez S. 2014. Neurobiological foundations of multi-sensory integration in people with autism spectrum disorders: the role of the medial prefrontal cortex. *Front Hum Neurosci.* 8:970.
- Maximo JO, Keown CL, Nair A, Müller R-A. 2013. Approaches to local connectivity in autism using resting state functional connectivity MRI. *Front Hum Neurosci.* 7:605.
- Mottershead JP, Schmierer K, Clemence M, Thornton JS, Scaravilli F, Barker GJ, Tofts PS, Newcombe J, Cuzner ML, Ordidge RJ, et al. 2003. High field MRI correlates of myelin content and axonal density in multiple sclerosis. *J Neurol.* 250:1293–1301.
- Nasrallah FA, Tay HC, Chuang KH. 2014. Detection of functional connectivity in the resting mouse brain. *NeuroImage.* 1: 417–424.
- Oguz I, Zhang H, Rumple A, Sonka M. 2014. RATS: rapid automatic tissue segmentation in rodent brain MRI. *J Neurosci Methods.* 221:175–182.
- Öngür D, Price J. 2000. The organization of networks within the orbital and medial prefrontal cortex of rats, monkeys and humans. *Cereb Cortex.* 10:206–219.
- Osakada F, Callaway EM. 2013. Design and generation of recombinant rabies virus vectors. *Nat Protoc.* 8:1583–1601.
- Paxinos G, Franklin K. 2011. *The mouse brain in stereotaxic coordinates.* 1st ed. Sydney: Academic Press.
- Peñagarikano O, Abrahams BS, Herman EI, Winden KD, Gdalyahu A, Dong H, Sonnenblick LI, Gruver R, Almajano J, Bragin A, et al. 2011. Absence of CNTNAP2 leads to epilepsy, neuronal migration abnormalities, and core autism-related deficits. *Cell.* 147:235–246.
- Poliak S, Salomon D, Elhanany H, Sabanay H, Kiernan B, Pevny L, Stewart CL, Xu X, Chiu SY, Shrager P, et al. 2003. Juxtaparanodal clustering of Shaker-like K<sup>+</sup> channels in myelinated axons depends on Caspr2 and TAG-1. *J Cell Biol.* 162: 1149–1160.
- Rane P, Cochran D, Hodge SM, Haselgrove C, Kennedy DN, Frazier JA. 2015. Connectivity in autism: a review of MRI connectivity studies. *Harv Rev Psychiatry.* 23:223–244.
- Riccomagno MM, Kolodkin AL. 2015. Sculpting neural circuits by axon and dendrite pruning. *Annu Rev Cell Dev Biol.* 31: 779–805.
- Richetto J, Chesters R, Cattaneo A, Labouesse MA, Gutierrez AMC, Wood TC, Luoni A, Meyer U, Vernon A, Riva MA. 2016. Genome-wide transcriptional profiling and structural magnetic resonance imaging in the maternal immune activation model of neurodevelopmental disorders. *Cereb Cortex.* [Epub ahead of print].
- Rodenas-Cuadrado P, Ho J, Vernes SC. 2014. Shining a light on CNTNAP2: complex functions to complex disorders. *Eur J Hum Genet.* 22:171–178.
- Sanders SJ, He X, Willsey AJ, Ercan-Sencicek AG, Samocha KE, Cicek AE, Murtha MT, Bal VH, Bishop SL, Dong S, et al. 2015. Insights into autism spectrum disorder genomic architecture and biology from 71 risk loci. *Neuron.* 87:1215–1233.
- Scattoni ML, Ricceri L, Crawley JN. 2011. Unusual repertoire of vocalizations in adult BTBR T+tf/J mice during three types of social encounters. *Genes Brain Behav.* 10:44–56.
- Scattoni ML, Gandhi SU, Ricceri L, Crawley JN. 2008. Unusual repertoire of vocalizations in the BTBR T+tf/J mouse model of autism. *PLoS ONE.* 3:e3067.
- Scattoni ML, Martire A, Cartocci G, Ferrante A, Ricceri L. 2013. Reduced social interaction, behavioural flexibility and BDNF signalling in the BTBR T+tf/J strain, a mouse model of autism. *Behav Brain Res.* 251:35–40.
- Schreiner MJ, Karlsgodt KH, Uddin LQ, Chow C, Congdon E, Jalbrzikowski M, Bearden CE. 2014. Default mode network connectivity and reciprocal social behavior in 22q11.2 deletion syndrome. *Soc Cogn Affect Neurosci.* 9:1261–1267.
- Scholz J, Klein MC, Behrens TEJ, Johansen-Berg H. 2009. Training induces changes in white-matter architecture. *Nat Neurosci.* 12:1370–1371.
- Scott-Van Zeeland AA, Abrahams BS, Alvarez-Retuerto AI, Sonnenblick LI, Rudie JD, Ghahremani D, Mumford JA, Poldrack RA, Dapretto M, Geschwind DH, et al. 2010. Altered functional connectivity in frontal lobe circuits is associated with variation in the autism risk gene CNTNAP2. *Sci Transl Med.* 2:56ra80.
- Sforazzini F, Schwarz AJ, Galbusera A, Bifone A, Gozzi A. 2014. Distributed BOLD and CBV-weighted resting-state networks in the mouse brain. *NeuroImage.* 87:403–415.
- Sforazzini F, Bertero A, Doderio L, David G, Galbusera A, Scattoni ML, Pasqualetti M, Gozzi A. 2016. Altered functional connectivity networks in allosal and socially impaired BTBR mice. *Brain Struct Funct.* 221:941–954.
- Steffey MA, Brosnan RJ, Steffey EP. 2003. Assessment of halothane and sevoflurane anesthesia in spontaneously breathing rats. *Am J Vet Res.* 64:470–474.
- Strauss KA, Puffenberger EG, Huentelman MJ, Gottlieb S, Dobrin SE, Parod JM, Stephan DA, Morton DH. 2006. Recessive symptomatic focal epilepsy and mutant contactin-associated protein-like 2. *N Engl J Med.* 354:1370–1377.
- Sun T, Hevner RF. 2014. Growth and folding of the mammalian cerebral cortex: from molecules to malformations. *Nat Rev Neurosci.* 15:217–232.
- Supekar K, Uddin LQ, Prater K, Amin H, Greicius MD, Menon V. 2010. Development of functional and structural connectivity within the default mode network in young children. *NeuroImage.* 52:290–301.
- Tan GCY, Doke TF, Ashburner J, Wood NW, Frackowiak RSJ. 2010. Normal variation in fronto-occipital circuitry and cerebellar structure with an autism-associated polymorphism of CNTNAP2. *NeuroImage.* 53:1030–1042.
- Tang G, Gudsnuk K, Kuo SH, Cotrina ML, Rosoklija G, Sosunov A, Sonders MS, Kanter E, Castagna C, Yamamoto A, Yue Z, Arancio O, et al. 2014. Loss of mTOR-dependent macroautophagy causes autistic-like synaptic pruning deficits. *Neuron.* 83:1131–1143.
- Tournier JD, Calamante F, Connelly A. 2007. Robust determination of the fibre orientation distribution in diffusion MRI: Non-negativity constrained super-resolved spherical deconvolution. *Neuroimage.* 35:1459–1472.
- Tournier JD, Calamante F, Connelly A. 2012. MRtrix: diffusion tractography in crossing fiber regions. *Int J Imaging Syst Technol.* 22:53–66.

- Uddin LQ, Supekar K, Menon V. 2013. Reconceptualizing functional brain connectivity in autism from a developmental perspective. *Front Hum Neurosci.* 7:458.
- Vogt B, Paxinos G. 2014. Cytoarchitecture of mouse and rat cingulate cortex with human homologues. *Brain Struct Funct.* 219:185–192.
- Yushkevich PA, Piven J, Hazlett HC, Smith RG, Ho S, Gee JC, Gerig G. 2006. User-guided 3D active contour segmentation of anatomical structures: significantly improved efficiency and reliability. *NeuroImage.* 31:1116–1128.
- Zhan Y, Paolicelli R, Sforzini F, Weinhard L, Bolasco G, Pagani F, Vissosktsy A, Bifone A, Gozzi A, Ragozzino D, et al. 2014. Deficient neuron-microglia signaling results in impaired functional brain connectivity and social behavior. *Nat Neurosci.* 17: 400–406.

## Supplementary figures

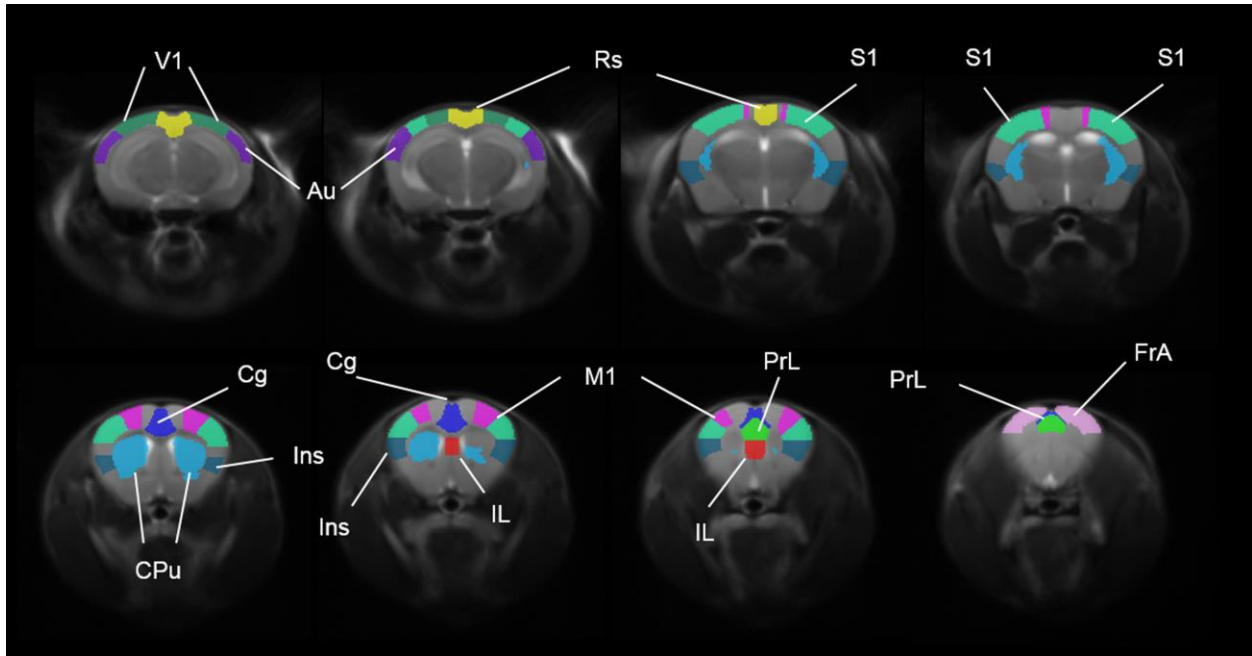


*Figure S1*

*Volumes of interest used in functional connectivity mappings.* V1, primary visual cortex; Au, auditory cortex; Rs, retrosplenial cortex; S1, primary somatosensory cortex; Cg, cingulate cortex; CPu, caudate-putamen; Ins, insular cortex; IL, infra-limbic cortex; M1, primary motor cortex; PrL, prelimbic cortex; FrA, frontal association cortex.

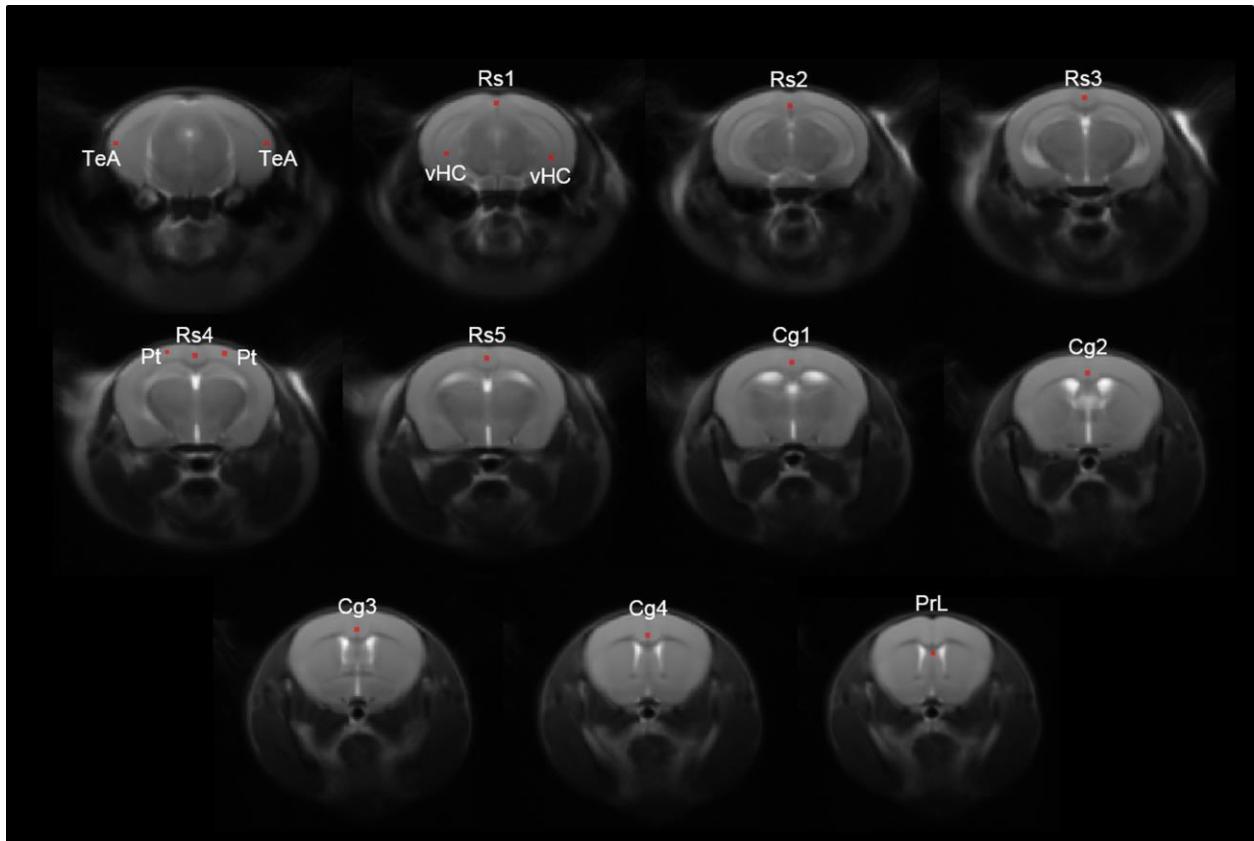
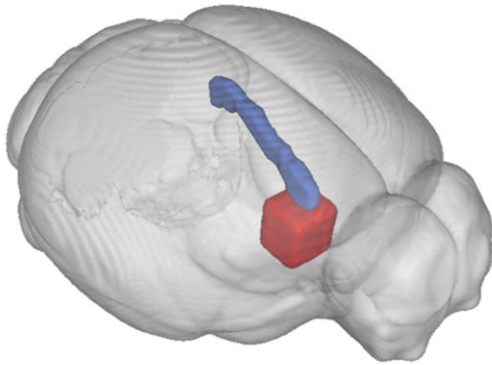


*Figure S2*

*Location of seeds used in mapping anteroposterior DMN connectivity.* TeA, temporal association cortex (bilateral); Rs, retrosplenial cortex; Cg, cingulate cortex; Pt, posterior parietal association cortex (bilateral); PrL, prelimbic cortex; vHC: ventral hippocampus.

Corpus callosum



Cingulum

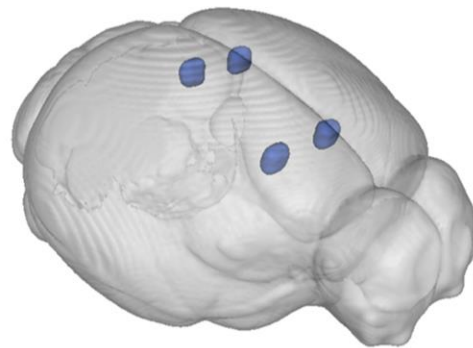


*Figure S3*

*Location of waypoint ROIs used for virtual dissection of corpus callosum and cingulum tracts from whole-brain white matter tractography. Inclusion ROIs are indicated in blue, exclusion ROIs are indicated in red.*

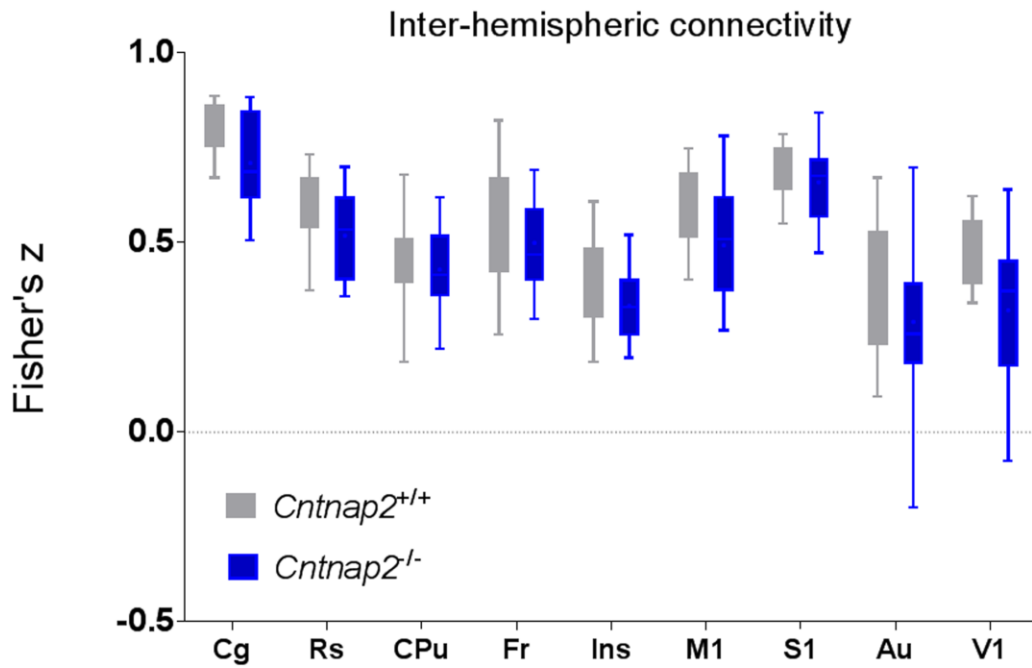
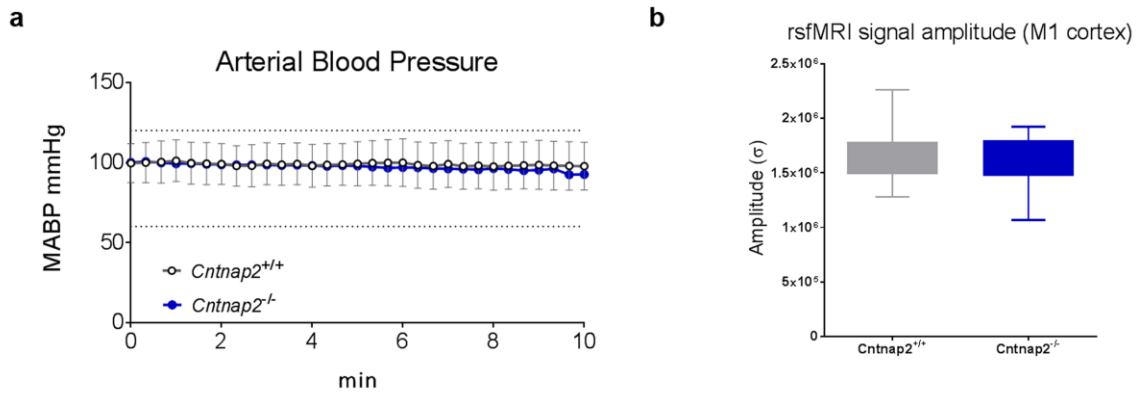


Figure S4

*Largely preserved inter-hemispheric connectivity in *Cntnap2*<sup>-/-</sup> mutants and control mice.*

Correlation coefficients were calculated between time courses extracted from VOIs depicted in Fig. S1 and the resulting *r*-scores were transformed to *z*-scores using Fisher's *r*-to-*z* transform.

None of these comparisons survived a false discovery rate correction at  $q = 0.05$ .



**Figure S5**

No genotype-dependent differences in anaesthesia sensitivity were detected as seen with mean arterial blood pressure mapping ( $t$ -test,  $t_{24} = 0.17$ ,  $p = 0.87$ ; **a**) and amplitude of cortical BOLD signal fluctuations in primary motor cortex ( $t$ -test,  $t_{24} = 0.72$ ,  $p = 0.48$ ; **b**). M1, primary motor cortex.

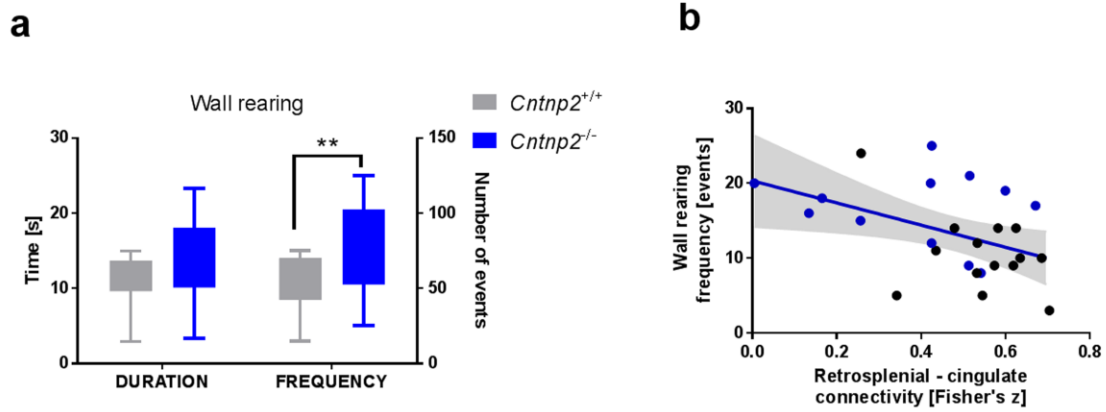


Figure S6

*Increased non-social behaviour in Cntnap2<sup>-/-</sup> mutants compared to control littermates.* (a) Non-social behaviour as measured by the duration and frequency of rearing up against the wall of the home-cage (frequency: *t*-test,  $t_{24} = 3.09$ ,  $p = 0.01$ ). (b) An inverse association between non-social behaviour and connectivity between retrosplenial and cingulate cortices (wall rearing, frequency:  $r = -0.45$ ,  $p = 0.02$ ,  $n = 26$ ,  $R^2 = 0.21$ ). \*  $p < 0.05$ , \*\*  $p < 0.01$ .

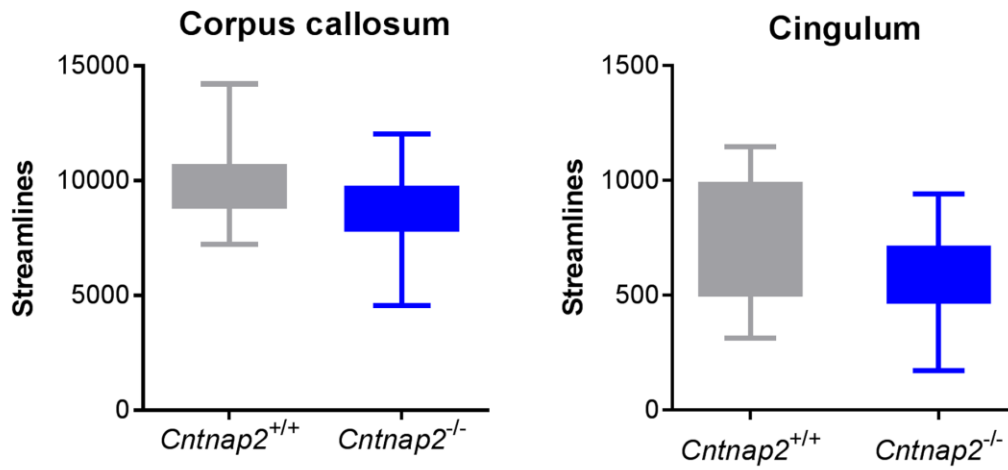
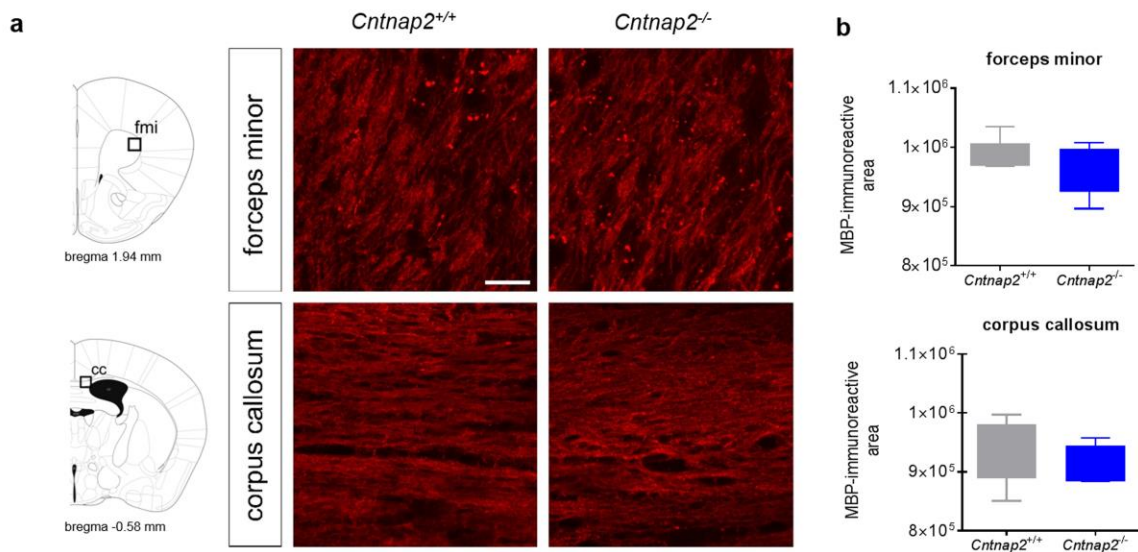


Figure S7

*White-matter tractography-based streamline counts.* Numbers of streamlines in corpus callosum and cingulum showed no significant differences between the *Cntnap2*<sup>-/-</sup> and control littermates (cingulum: *t*-test,  $t_{21} = 1.25$ ,  $p = 0.23$ ; corpus callosum: *t*-test,  $t_{21} = 1.21$ ,  $p = 0.24$ ).



**Figure S8**

*Histological and immunohistochemical analysis of white matter.* (a) Representative images of anterior callosal regions characterized by parallel or transversal fibre extension with respect to the imaging plane (corpus callosum and forceps minor of the corpus callosum, respectively). No apparent difference in fibre organization or MBP stained regions was observed between genotypes. (b) MBP-immunoreactive area averaged from three random image fields per region and animal ( $n = 5$ , each group; corpus callosum:  $t$ -test,  $t_8 = 0.84$ ,  $p = 0.42$ ; forceps minor of the corpus callosum:  $t$ -test,  $t_8 = 1.06$ ,  $p = 0.32$ ).